ELSEVIER

Contents lists available at ScienceDirect

Journal of Catalysis

journal homepage: www.elsevier.com/locate/jcat





Dynamic interactions between adsorbates and catalyst surfaces over long-term OER stability testing in acidic media

Ruihan Li, Bingzhang Lu, Jane Edgington, Linsey C. Seitz

Department of Chemical and Biological Engineering, Northwestern University, Evanston, IL 60208-3113, United States

ARTICLE INFO

Keywords: Electrocatalysis Oxygen Evolution Reaction Iridium Surface Adsorbates Stability Dynamic Materials

ABSTRACT

The interaction between catalyst surfaces and adsorbed oxygen intermediates is critical to catalytic performance for electrochemical water oxidation to oxygen. However, the relationship between adsorption energetics and electrocatalytic activity is primarily assessed for pristine catalyst materials, which leaves much unknown about the dynamics of these properties in relationship to catalyst performance during long-term operation. In this work, we experimentally assess OH and O adsorption on Ca₂IrO₄ nanoparticles and monitor their evolution during extensive chronoamperometry tests at highly oxidizing potentials in a range of low pH electrolytes. *In situ* x-ray absorption spectroscopy reveals changes for surface adsorbate energetics and local iridium structures with applied potentials. Increasingly unfavorable adsorption of OH and formation of O intermediates after long-term operation is correlated with severe metal dissolution, distorted [IrO₆] octahedral linkages, and a decreased average Ir valence. This work establishes connections between surface adsorption energetics, Ir structure, OER kinetics, and material stability outcomes.

1. Introduction

Polymer electrolyte membrane (PEM) water electrolysis is a potentially transformative technology for hydrogen production that boasts high energy efficiency, rapid system response, and a large partial load range.[1,2] The anodic reaction, where the oxidation of water or the oxygen evolution reaction (OER) occurs, requires carefully tuned active and stable catalysts because of the sluggish kinetics of the 4-electron OER process. Considering the OER intermediates *OH, *O, and *OOH in the proposed proton-concerted-electron-transfer (PCET) steps, the electrocatalytic activity is determined by the surface binding energy following the Sabatier principle: the material that binds these oxygen intermediates on its surface neither too strongly nor too weakly achieves the highest OER performance.[3-5] Iridium-based metal oxides (i.e., $A_{n+1}Ir_nO_{3n+1}$, A = Sr, Ca, Ba, n = 1 to ∞) are among the most promising materials for OER in acidic media, due to their balance of high activity and reasonable stability at low pH.[6-11] Understanding how oxygen intermediates affect chemical properties of surface iridates is critical for rational design of these materials to achieve optimal binding with oxygenates, which in turn influences intrinsic OER activity.

Current work mostly focuses on identifying or estimating the potential for OH/O adsorption on a limited range of iridium-based oxide

systems. For instance, experimental work on IrO₂ shows OH adsorption at ~ 0.77 V vs. RHE (V_{RHE}) in acid, [12] while H_{3.6}IrO₄·3.7H₂O undergoes an intercalation of H_3O^+ within the layered iridate at ~ 0.92 V_{RHE} followed by deprotonation into *O at ~ 1.14 V_{RHE} .[13] Theoretical work reveals that *OH and *O adsorb on the rutile IrO2 (110) facet at $0.92\ V_{RHE}$ and $1.31\ V_{RHE}$ in alkaline, respectively.[14] This facet is also calculated to become completely hydroxylated (i.e. *OH adsorbates terminating the surface) at potentials $< 1.2 \ V_{RHE}$ in acid.[15] Although theoretical work provides estimations of single crystalline oxide counterparts, this approach is challenging for the investigation of more applied polycrystalline iridates since each facet renders different binding energies of oxygenates. Depending on the surrounding electrolyte environment and applied potentials, surface adsorbate coverage and iridate structure experience constant changes.[8,10,11,14,16–18] However, detailed analyses relating variation of surface adsorption energetics with the dynamic nature of iridium moieties in active catalysts remain scant or inconclusive. Additionally, the evolution of oxygen adsorbate interactions with catalyst surfaces has not been investigated during long-term OER, when significant surface reconstruction is induced by prolonged exposure to extreme pH and high potential. Therefore, a systematic study to unravel the correlation between oxygenate adsorption, surface iridate structure, and long-term OER

E-mail address: linsey.seitz@northwestern.edu (L.C. Seitz).

 $^{^{\}ast}$ Corresponding author.

performance will enable researchers to tune reaction conditions to balance catalyst activity and long-term stability.

Ca₂IrO₄ exhibits a typical activity evolution of OER, with increasing activity during initial testing followed by a stable period and eventual activity decline, but a shorter lifespan compared to many other iridates, [8] making it a convenient material platform to observe varying adsorption behaviors and stability outcomes and relate them to dynamic structural properties of iridate. The overall activity and material dynamic trends observed here match several examples of iridate materials studied for acidic OER in literature. [8,10,17,19] Building upon this idea, we adopted Ca₂IrO₄ nanoparticles to investigate the interactions between oxygen adsorbates and the catalyst surface during long-term OER operation, ensuring the adsorption features are monitored during both phases of electrode activation and degradation. A combination of in situ and ex situ X-ray absorption spectroscopy (XAS) as well as inductively coupled plasma mass spectrometry (ICP-MS) are employed to probe catalyst material responses to applied potentials and operating time. Our rigorous electrochemical testing also brings to light pH-dependent adsorption energetics, revealing tunable oxygen adsorbate interactions with catalyst surfaces in various chemical environments.

2. Results and discussion

2.1. OH/O adsorption on Ca2IrO4 nanoparticles

X-ray diffraction (XRD, Fig. 1a) and high-resolution transmission electron microscopy (HRTEM, Fig. 1b) were used to obtain both global and local information of the pristine material, respectively. XRD confirms the hexagonal crystal structure of $\text{Ca}_2\text{IrO}_4\text{[20]}$ and a pure crystalline bulk phase achieved by Pechini synthesis (details provided in SI). HRTEM shows that the as-prepared nanoparticles are composed of a crystalline bulk phase (\sim 30 nm) covered by several nanometers of small grains (Fig. 1b and Fig. S2). The diffused halo ring feature in the diffraction pattern also confirms that no long-range-order materials exist on the surface.

Similar to techniques previously used to determine OH/O adsorption on IrO₂(110) and RuO₂(110),[14,21] we conducted rapid (200 mV/s) cyclic voltammetry (CV) to measure the adsorption energies of *OH and *O adsorbates. Specifically, the catalyst was cycled in a potential range preceding OER ($\sim\!0.3~V-1.4~V_{RHE})$ in Ar-saturated 0.1 M HClO₄. We note that the catalyst surface site heterogeneity of our material results in broadened adsorption peaks, which precludes precise analysis of features (i.e., charge, FWHM[21]) resulting from interactions between adsorbates and homogeneous sites, as is possible on single crystals or thin films with controlled facet exposure. The observed electroadsorption results from an ensemble of placement of adsorbates on

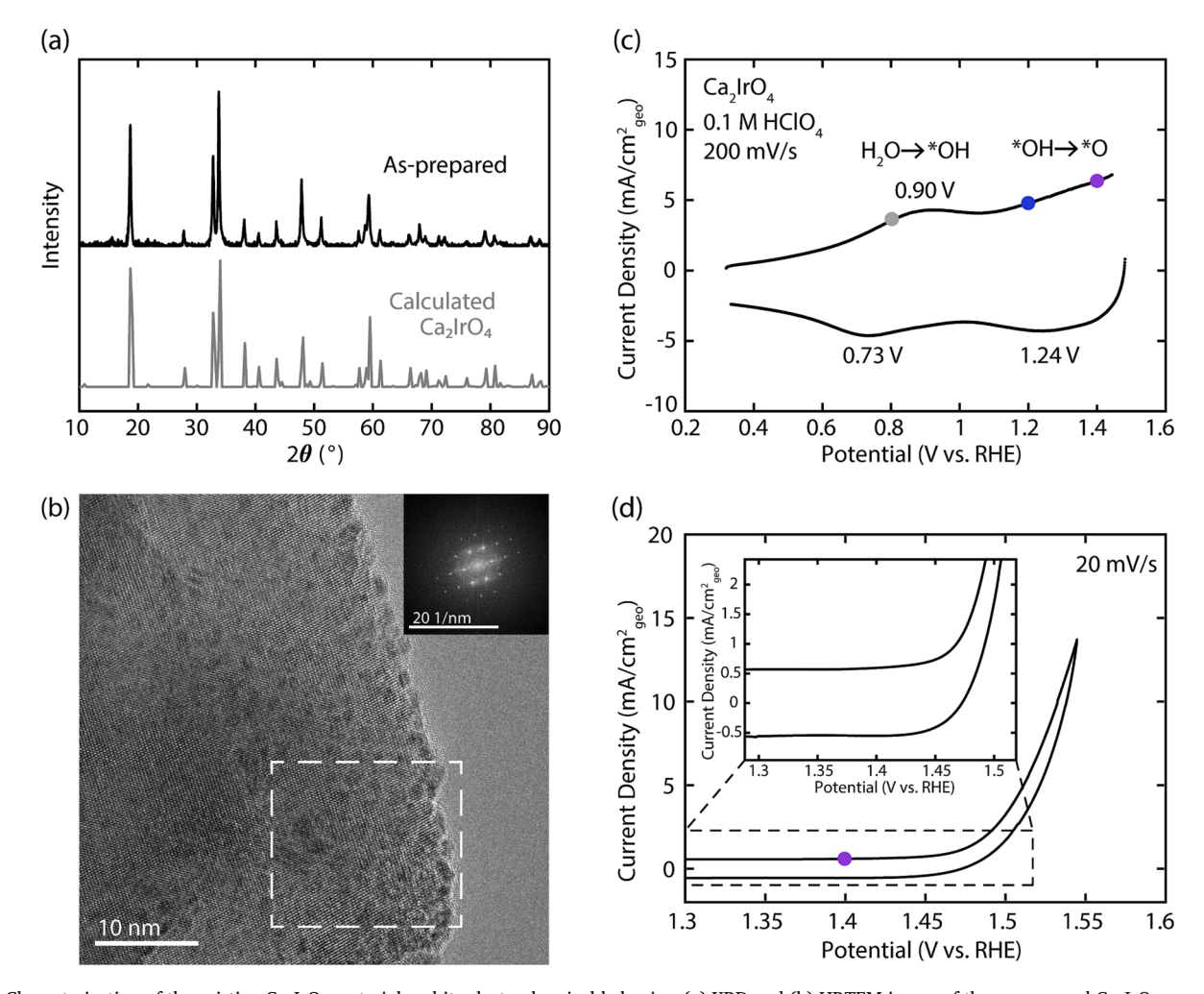


Fig. 1. Characterization of the pristine Ca_2IrO_4 material and its electrochemical behavior. (a) XRD and (b) HRTEM image of the as-prepared Ca_2IrO_4 nanoparticles with insets showing the Fast Fourier Transform of the highlighted region. (c) Rapid CV of Ca_2IrO_4 at a scan rate of 200 mV/s with 10 s holds at vertex potentials. (d) CV of Ca_2IrO_4 over OER-relevant potentials at a scan rate of 20 mV/s with inset showing no redox peaks within this range. Colored points in c and d identify potentials selected for *in situ* XAS measurement before OER onset.

heterogenous sites. Two broad peaks are observed in anodic/cathodic scan (Fig. 1c). The first peak is visible at \sim 0.90 V_{RHE} in the anodically swept direction (or \sim 0.73 V_{RHE} cathodically) and the second peak appears at \sim 1.24 V_{RHE} . The electrochemical potentials correspond to the free energies of oxygen intermediates and these peaks that precede OER current onset are assigned to OH and O adsorption, as shown. The position of the OH adsorption peak corresponds to the binding energy of *OH, and the position of O adsorption peak reflects the reaction free energy of the *OH deprotonation step to form *O. OER is found to onset after 1.48 V_{RHE} upon cycling the catalyst in a wider potential window that clearly reveals Faradaic reaction current, eventually reaching a useful benchmark current density of 10 mA/cm $_{\rm geo}^2$ at an overpotential of 305 mV (Fig. 1d).

2.2. Dynamic surface adsorption and Ir structure with applied potentials

Using this initial redox behavior as a guide, we conducted *in situ* XAS at the following potentials to probe the impact of adsorbates and catalytic activity: 0.8 (OH adsorbates), 1.2 (O adsorbates), 1.4 (just before OER onset), 1.576, and 1.6 $V_{\rm RHE}$ (both OER kinetic regime and OOH adsorbates). At these selected potentials we investigate how oxygen adsorbate – catalyst surface interactions vary under applied potential and changes in Ir structure. *In situ* X-ray absorption near edge structure (XANES, Fig. 2) at the Ir-L_{III} edge was employed to monitor the electronic state of Ir while extended X-ray absorption fine structure (EXAFS, Fig. S3) was recorded simultaneously to understand the geometric structure change of the Ir first shell under selected potentials. The small

size of nanoparticles renders a relatively high surface-to-volume ratio so that the information obtained by this bulk-sensitive technique estimates near-surface bulk information.

XANES spectra are strongly influenced by the local electronic structure and configuration of the absorbing atom.[22] XANES white line (WL) positions reflect the average electron transition energy from core-level 2p to unoccupied 5d states. As the applied potential is increased from 0.8 to 1.2 V_{RHE}, corresponding to a surface adsorbate coverage change from *OH to *O, we observe significant changes in the WL position, which shifts ~ 0.4 eV to higher energy (Fig. 2b). WL position is further shifted by $\sim 0.3\ eV$ when the potential is further increased to 1.4 V_{RHE} . The XANES WL position remains consistent upon further increasing the oxidizing potential to 1.6 V_{RHE}. Next, the XANES edge energy positions reflect the lowest energy required to enable an electron transition from core-level 2p to unoccupied 5d states. Following the trends in edge energy position with respect to the white line position, one can also estimate the broadening of the white line peak, which reflects heterogeneity of 5d occupancy among the probed Ir sites. As the applied potential is increased from 0.8 to 1.2 V_{RHE}, the edge energy shifts to higher energy, mirroring the WL shift at these potentials. However, upon increasing the potential to 1.4 and 1.576 V_{RHE} , the edge energy and WL position trends bifurcate such that the edge position shifts back to lower energy, resulting in a broadened WL peak. At the highest potential, 1.6 V_{RHE}, the edge energy position reaches its highest level, reflecting the highest valence state (\sim 4.0 +), in parallel with a narrowing of the WL peak. At these same potentials, EXAFS reveals that the initial, average Ir-O bond length of surface and bulk Ir atoms is 2.00

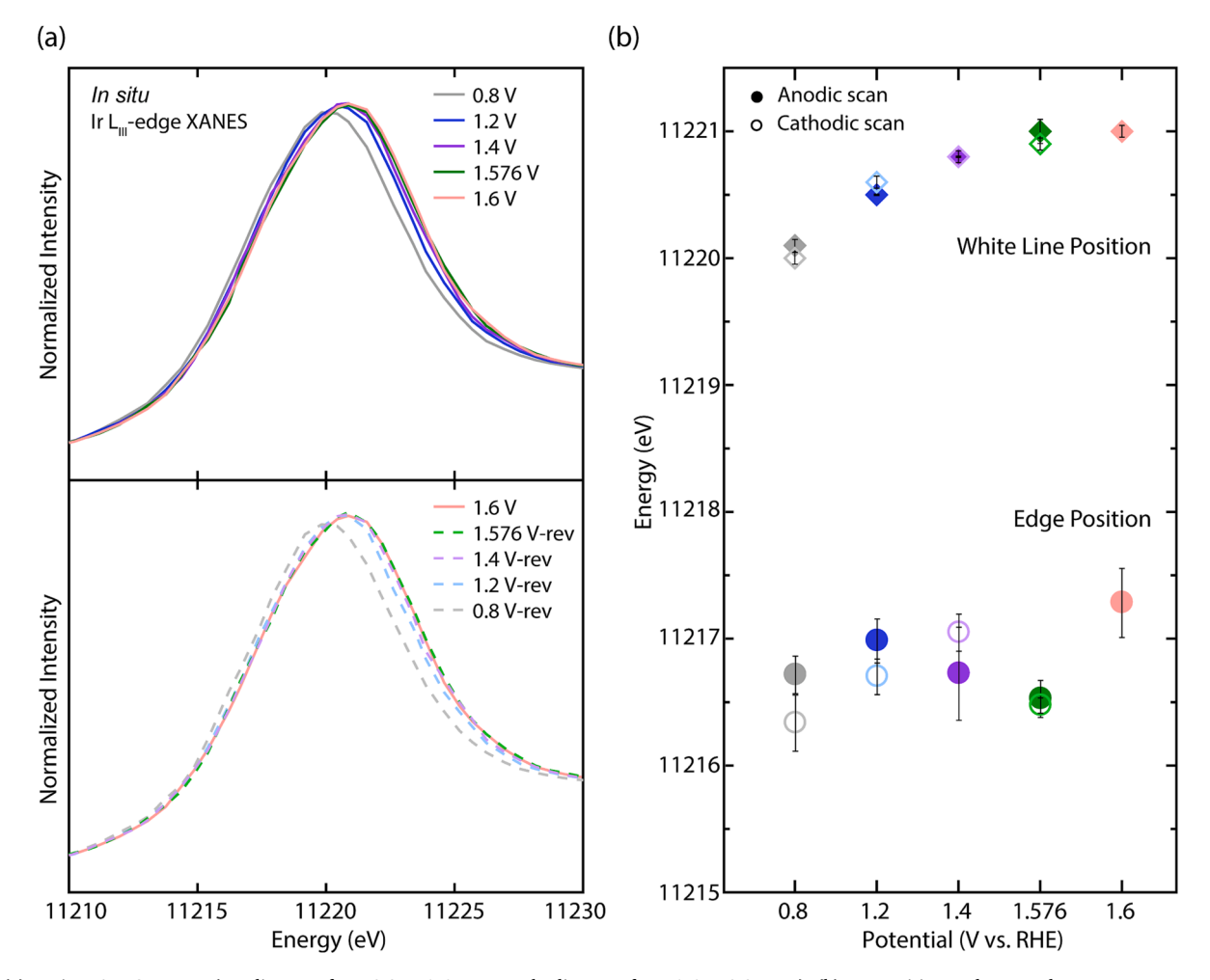


Fig. 2. (a) In situ XANES spectra (anodic scan: from 0.8 to 1.6 V_{RHE}; cathodic scan: from 1.6 to 0.8 V_{RHE}). (b) WL position and Ir L_{III} edge energy at corresponding potentials with error bars showing the standard deviation of two scans and a merged scan. The sample was measured in fluorescence mode.

Å at 0.8 and 1.2 V_{RHE} (Table S1), which is then decreased to 1.97 Å when the potential is increased to 1.4 V_{RHE} . EXAFS spectra and average Ir-O bond lengths remain consistent upon further increasing the oxidizing potential to 1.6 V_{RHE} .

In addition to tracking changes in Ir structure with increasingly anodic applied potentials that simulate the anodic scan of a CV, we subsequently step-wise reduced the applied potential back to 0.8 V_{RHE} (Fig. 2b) to observe if the Ir structural changes discussed above are reversible during a cathodic scan. Similarly, a significant, overall, negative shift in XANES spectra and an elongated Ir-O bond are observed as the potential is reduced back to 0.8 V_{RHE} , reflecting the protonation step from *O to *OH that occurs between 1.2 and 0.8 V_{RHE} . The overlapping XANES spectra and similar EXAFS fit results of anodically and cathodically stepped potentials suggest a reversible process.

We therefore hypothesize that the increasing WL positions for samples measured under applied potentials from 0.8 to 1.2 V_{RHE} might be caused by changes in the electronic structure and local bonding of Ir

associated with surface adsorbate deprotonation that results in a higher average electron 2p to 5d transition energy. As the potential approaches OER onset, some Ir-based materials have been found to show $Ir^{4+ \rightarrow 5+}$ redox peaks at $\sim 1.4 \text{ V}_{\text{RHE}}[10,13,23]$ however this feature is not observed for our catalyst (Fig. 1d). Instead, we hypothesize that the increasing surface *O coverage from 1.2 to 1.4 V_{RHE} may further increase the average 2p to 5d electron transition energy in Ir, inducing a positive shift in WL energy position. Furthermore, the broadening of the WL peak at 1.4 and 1.576 V_{RHE} may reflect the heterogeneous nature of available Ir surface sites that support a range of adsorbate binding energies and result in a broadened ensemble of Ir valence states upon increased surface adsorption; the WL peak narrowing at the highest potential (1.6 V_{RHE}) may then reflect an operating condition where a sufficiently high voltage is supplied to activate and increase the valence state for a majority of Ir sites, thereby reducing site heterogeneity under these conditions. Additionally, EXAFS fitting results indicate a shorter average Ir-O bond as the material experiences increasingly oxidative

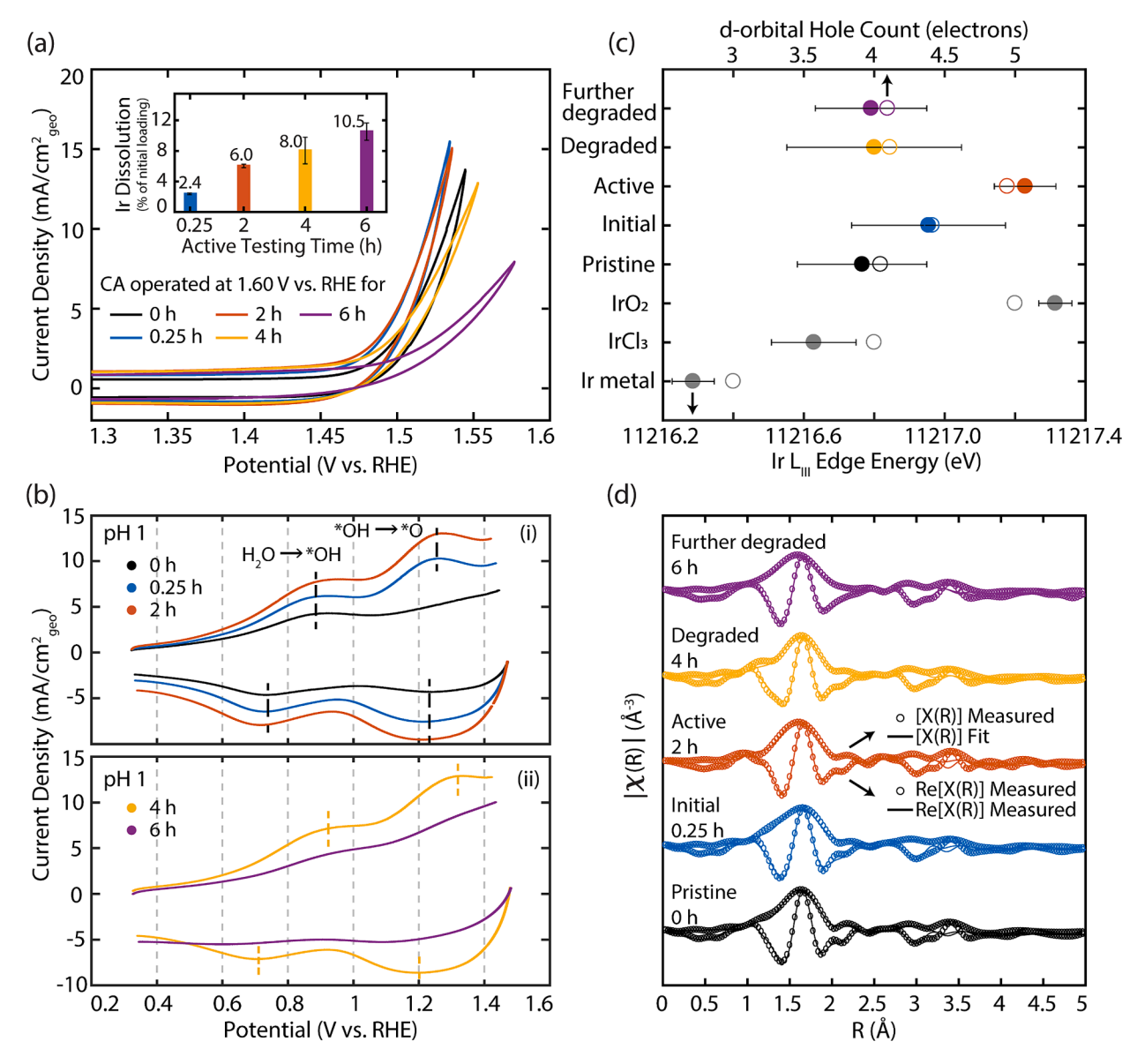


Fig. 3. (a) Geometric activity with inset showing Ir dissolution as a function of testing time (presented as percentage of initial loading at 15.68 μg_{II} ; error bars show the standard deviation of three measurements), and (b) surface adsorption after denoted time of CA at 1.60 V_{RHE} in 0.1 M HClO₄. Dashed vertical lines guide the eye for adsorption peak positions. (c) Edge energy (solid markers) obtained from *ex situ* XANES with error bars showing the standard deviation of four scans and calculated d-orbital occupancy (open markers) (0 h – pristine, 0.25 h – initial, 2 h – active, 4 h – degraded, 6 h – further degraded), the uncertainty in edge position is ~ 0.5 eV for this data set. (d) *Ex situ* EXAFS experimental spectra and fits.

applied potentials from 1.2 to 1.4 V_{RHE} , suggesting a stronger binding of oxygen to Ir. The increasing surface *O coverage is hypothesized to reduce the observed average bond length of Ir-O, albeit to a small extent, while the bulk remains pristine geometric structure with an Ir-O bond length of 2.00 Å.

Collectively, our results show that Ir experiences changes in electronic and geometric structure at applied potentials prior to driving the overall OER. The dynamic Ir structural change can be summarized via the following five stages: 1) increase in average electron 2p to 5d transition energy induced by the transition in surface coverage from OH to O adsorbates, 2) decrease in average Ir-O bond length with increasing O adsorbate coverage before OER onset, 3) stabilization of average Ir-O bond length with increased heterogeneous Ir sites that support a diverse ensemble of adsorbates placements during OER, 4) an increase in average Ir valence and a decrease in site heterogeneity for surface adsorption at sufficiently high potential, and 5) a reversible Ir structural change due to protonation/deprotonation of oxygenates upon application of increasingly cathodic potentials simulating the reverse CV sweep.

2.3. OH/O adsorption and Ir structure during long-term stability testing

To further investigate how catalyst surface - oxygen adsorbate interactions change during long-term operation, we applied stability protocols that alternate extended chronoamperometric holds (CAs at 1.60 V_{RHE}) with cyclic voltammetry (CVs) of electrodes in 0.1 M HClO₄ over 6 h, ensuring that oxygenate adsorption would be probed during both activation and deactivation processes of the catalyst. The evolution of geometric activity (obtained with slow CVs conducted at 20 mV/s over the faradaic region) and surface adsorption (obtained by rapid CVs at 200 mV/s) are shown in Fig. 3a-b. In the first CV, the catalyst requires only 305 mV overpotential to reach 10 mA/cm_{geo}; the activity then swiftly increases over the first 0.25 h of testing and is stable at this level for 2 h. The geometric activity then slowly decreases in a third phase after 4 h and 6 h of testing. During the initial OER testing phase, designated with the label "0.25 h", two adsorption peaks located at \sim 0.90 and \sim 1.25 V_{RHE} are clearly observed. During the second, stable "active" phase (2 h) for at least two hours, the electrode exhibits a growth in adsorption peak intensities but a negligible change in peak positions (Fig. 3b(i)), followed by a decrease in peak intensity and an anodic peak shift (\sim 0.06 V_{RHE}) occurring after the 4 h CA (Fig. 3b(ii)). Further degradation (6 h CA) leads to significant loss of peak intensity and adsorption features that are barely observable and difficult to accurately quantify their location.

To analyze these trends, we employ electrochemical capacitance to estimate the change in electrochemically accessible catalyst surface area (ECSA), which we compare with changes in surface adsorbate behavior and OER activity. While capacitance is broadly used in literature to reflect changes in catalyst surface area and significant surface rearrangement, [8,11,24,25] we note that capacitance may also vary with material intrinsic properties such as surface structure, composition, and conductivity. Changes in catalyst conductivity during electrochemical testing or the oxidation of the Vulcan carbon support or glassy carbon substrate can obstruct the conductive path between the catalyst and the electrode contact.[26,27] Nonetheless, many previous studies on Irbased materials have used this technique to show an increase in ECSA during catalyst activation. [8,11,24,25] Following this approach, we also note mirroring behavior of the geometric current density and capacitance, such that increasing and decreasing activity roughly follows increasing and decreasing capacitance, as demonstrated by capacitancenormalized CVs and overpotential required to reach 10 mA/cm²_{geo} (Fig. S4).

However, there is an even stronger correlation between geometric current density and surface adsorbate behavior. As we encounter challenges in resolving a distinct peak corresponding to the deprotonation step at 0 h and 6 h, our analysis for surface adsorbate behavior focuses solely on the charge associated with OH adsorption (i.e. integrated area

under the peak), serving as an indicator of the surface coverage of OH adsorbates (Fig. S4). When comparing the overpotential to reach 10 mA/cm²_{geo}, electrochemical capacitance, and OH_{ads} peak charge as a function of active testing time, all three of these metrics track very closely, with a slightly greater (inverse) agreement between overpotential and OHads peak charge compared to overpotential and capacitance. A primary difference is observed when the catalyst activity declines and the overpotential increases from 2 to 4 h testing, which is directly mirrored by a decline in the OHads peak charge, whereas the capacitance decreases more slowly from 2 to 6 h testing. Overall, the growing OH_{ads} peak magnitudes (0 - 2 h) indicate an increasing quantity of adsorbates that are able to bind to an increasing number of electrochemically accessible sites during activation. The depressed OH_{ads} adsorption peaks observed after 4 h CA then reflect a decrease in the number of surface adsorbates. It is important to note that the diminishing accessible sites do not account for all the changes in activity and surface coverage of adsorbates. According to the PCET steps of OER in acid $(H_2O^* \rightarrow {}^*OH + H^+ + e^-)$ and ${}^*OH \rightarrow {}^*O + H^+ + e^-)$, the free energy difference between OH and O adsorptions (often represented as ΔG_{O^*} – ΔG_{OH^*} in computational studies) corresponds to the peak position of O adsorption. [21] The shift of O adsorption peak to a higher potential after 4 h CA indicates an unfavorable deprotonation step, which arises from a more difficult OH adsorption as shown by the positive shift of the first adsorption peak at 4 h. Together, these unfavorable catalyst surface oxygenate absorbate interactions impede OER kinetics. Further degradation (6 h) leads to fewer electrochemically accessible sites or sites that are more heterogeneous such that the inactive surface is unable to bind a significant population of oxygenates or binds them over a wider range of potentials, resulting in barely visible, broadened adsorption peaks.

To understand how the reconstructed catalyst surface influences iridium binding with oxygenates over extended testing time, we also used a combination of ex situ techniques to characterize Ir after exposing catalysts to the corresponding reaction conditions. Specifically, ICP-MS (inset of Fig. 3a), XANES at the Ir-L_{III} edge (Fig. 3c, Fig. S5a), and EXAFS with Fourier transform analysis (Fig. 3d, Table S2) were carried out to track changes in the Ir dissolution, average Ir oxidation state, and geometric structure, respectively. We take the XANES edge energy, defined by the zero crossing of the second derivative, as the metric for average Ir valence. During catalyst activation (0 - 2 h), we observe relatively fast iridium dissolution, up to 6 % of the initial Ir content, and an increasing Ir-L_{III} edge position (\sim 0.54 eV) corresponding to an increase in average oxidation state from $\sim 3.05 + \text{to} \sim 3.95 + \text{(Fig. S5b,c)}$, as well as a negligible change in Ir-Ir bond length (3.30 Å to 3.29 Å). In comparison, Ir dissolves at a much slower rate during degradation (1.25 % Ir/h over 4-6 h vs. 2.4 % Ir/h over 0-0.25 h), which is accompanied by a decrease in Ir-L_{III} edge position and average Ir oxidation state reaching ~ 3.10+; interestingly, these samples also reveal a decrease in Ir-Ir bond length (reaching 3.05 Å) accompanied by an increase in Ca-Ir bond length. As significant OER occurs, Ir-Ir and Ca-Ir bond lengths serve as indicators of geometric structural change. The Ir-Ir bond lengths detected for the degraded materials are much shorter compared to the average Ir-Ir bond length in rutile IrO₂ structure (where Ir-Ir bond length is 3.14 Å between edge-sharing octahedra). In addition, during degradation (4 - 6 h), the Ca₂IrO₄ materials have an average Ir-Ir bond length of 3.086 Å (vs. $3.294\,\text{Å}$ during activation at $0-2\,\text{h}$) and an average Ca-Ir bond length of $3.247~\mbox{\normalfont\AA}$ (vs. $3.172~\mbox{\normalfont\AA}$ during activation). Therefore, we hypothesize that the reconstructed phase formed during degradation may have a tilted edge-sharing [IrO₆] octahedra that is more similar to the structures found in edge-sharing octahedra of hollandite K_{0.25}IrO₂ with Ir-Ir bond lengths of 3.07 Å.[28] Collectively, these results also suggest that Ir valence does not directly influence oxygen adsorbate interactions with the catalyst surface. In particular, over the course of stability testing, we observe that the increasing quantity of Ir⁴⁺ species does not directly affect the binding energy of OH and O adsorbate during activation (0 – 2 h), while decreased composition of Ir⁴⁺ does coincide with unfavorable OH and O adsorption potential shifts during degradation (4 h). Instead,

the geometric structure of Ir plays a more significant role in affecting surface adsorption and hence, OER kinetics. This is demonstrated in Figure S5d which compares the OH adsorption peak position vs. the average Ir-Ir bond length and Ir valence of these samples during each activity phase; the OH adsorption peak position tracks strongly with Ir-Ir bond length with decreasing bond length correlating to an anodic shift in OH adsorption peak position. Overall, we found that during electrode activation, our material has increased composition of Ir in the 4 + state but stable edge-sharing [IrO₆] octahedra that relatively accelerates Ir leaching and exposes more sites for OH/O adsorption without affecting the binding energy to oxygenates. During degradation, the reconstructed material is increasingly composed of Ir³⁺ within a more compacted [IrO₆] linkage that mitigates aggressive Ir leaching and renders a high energy barrier to bind with oxygenates.

2.4. Catalyst surface – Oxygen adsorbate interactions in varied chemical environments

The electrode–electrolyte interface can be modulated by chemical environments with differences in ion mobility, electric field, and stability of Ir species. In this section, we study the catalyst surface – oxygen adsorbate interactions in a range of low pH electrolytes (pH 0 – 2). First, we look at the surface adsorption behaviors after immersing electrodes in electrolytes of varying acidic strength before CA holds (Fig. 4a and Fig. S7a). The pH 0 and 1 electrolytes contain only 1 M and 0.1 M HClO₄, whereas the pH 2 electrolyte contains 0.01 M HClO₄ with balance KClO₄

to achieve a total electrolyte concentration of 0.1 M (matching the ion concentration of the pH 1 electrolyte) to minimize ohmic drop. It has been observed that the ClO_4 does not lead to surface poisoning[21] or significant differences in adsorption peaks across low pH values[29] during short-term operation. However, the alkali cation (K^+) in pH 2 electrolyte may influence the electrified interfacial water, affecting the water structure near the electrode surface,[30] and possible accumulation of cations at the outer Helmholtz plane may increase the interfacial electric field, influencing the dipole moments and polarizabilities of intermediates.[31] However, in this system and with these ion concentrations, we expect these effects to be minor, especially considering the heterogeneity of sites present as compared to single crystal or facetcontrolled thin film studies where these effects may be more pronounced.

Fig. 3 shows that initial OH adsorption occurs at slightly more anodic potentials with increasing pH while O adsorption is not explicitly observable in all tested pHs, indicating that electrolyte pH does impact the energy of the adsorbed intermediates on Ca_2IrO_4 . In the context of other electrochemical reactions (i.e. CO reduction on Cu(211) and O_2 reduction on $Au(1\,0\,0)$), surface adsorbates have exhibited similar stabilization upon exposure to electrolytes of varying pH via different interfacial electric fields. [32–34] The adsorption peaks on Ca_2IrO_4 also slightly grow in intensity with increasing pH, reflecting a higher surface coverage of oxygenates which may be reflective of surface area or relative heterogeneity of available surface sites, as noted in the previous section. Since our electrodes are estimated to exhibit the same ECSA as

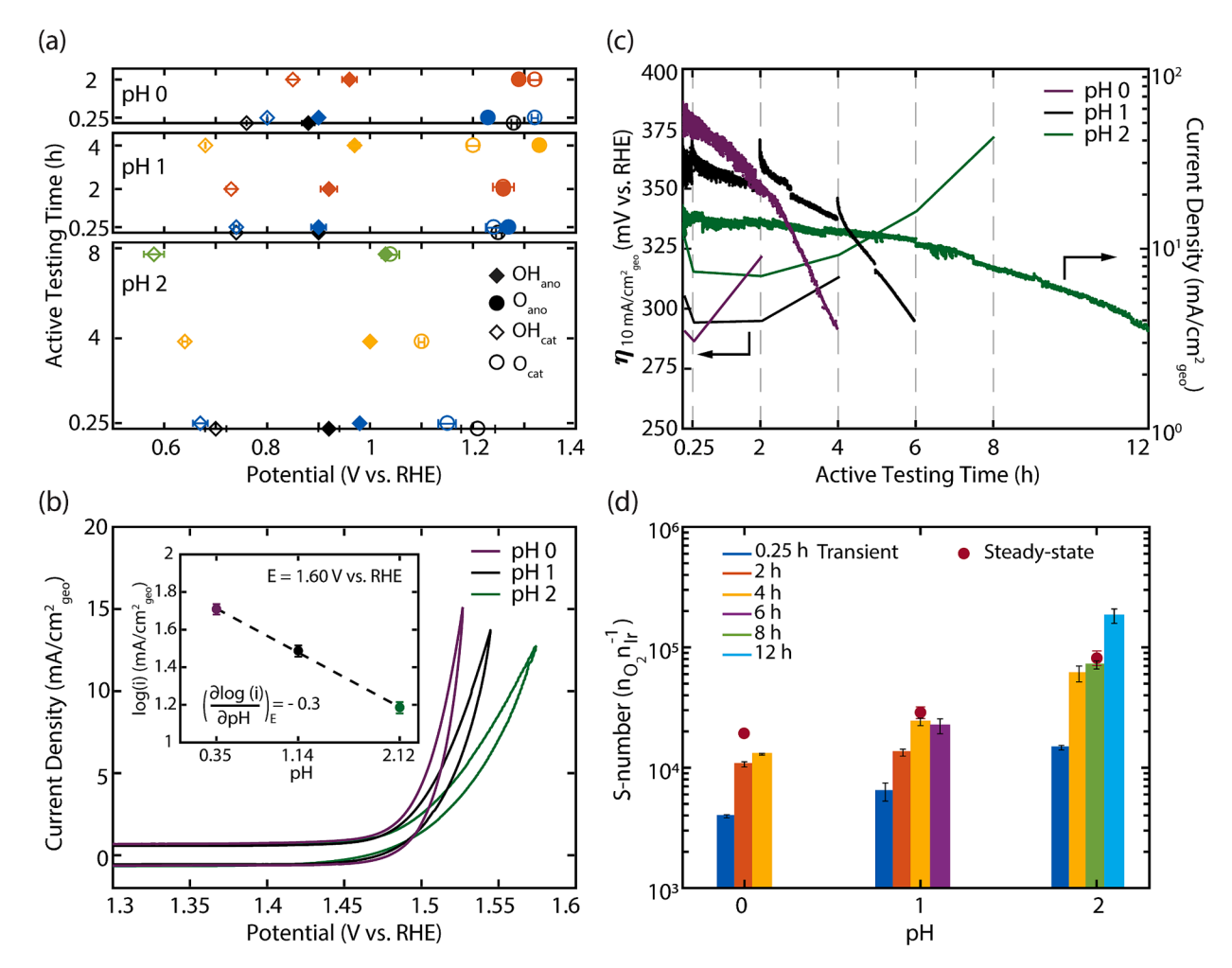


Fig. 4. (a) Adsorption peak positions in anodic and cathodic scans, (b) first CV scans showing geometric activity in various low pH electrolytes (\sim 0 h) with inset showing the stabilized currents at 1.60 V_{RHE}, (c) overpotential and stability as a function of active testing time during extensive CA. (d) S-numbers calculated from cumulative OER charge and Ir dissolved in varied HClO₄ solutions. Error bars show the standard deviation of three independent measurements.

indicated by the consistent capacitive currents in all tested pHs (Fig. 4b), the pH-dependent intensity of adsorption peaks is more likely due to increased catalyst surface site heterogeneity under low pH conditions. In addition, the relationship between pH, potential, and current is defined by the following equation:

$$i = k \bullet [H^+]^{-\rho} \bullet 10^{-\frac{\eta}{b}} \tag{1}$$

where ρ is reaction order, η is overpotential, and b is Tafel slope.[35] Based on this relationship between pH, potential, and current, the negligible reaction order (– 0.3 dec/pH) suggests a pH-independent PCET pathway in pH range 0 – 2,[36] indicating that the difference in OER activity is due to a compromise between binding energy of adsorbates (which affects η) and surface adsorbate coverage (which affects b). Since we observe an improvement in OER kinetics under lower pH conditions (Fig. 4b), our results show that the binding energy of the adsorbates, compared to surface coverage, plays a more important role in the pH-dependent OER activity.

Next, we monitor the evolution of oxygen adsorbate interactions with the catalyst surface during long-term stability testing. The same testing protocol was applied to the electrodes and the peak positions of OH and O adsorptions were assessed in HClO₄ electrolytes over 4 – 12 h ranging from pH 0 - 2 until each electrode lost > 80 % of its initial activity (Fig. 4a, Fig. S7b-d, Table S3). Compared to the distinct OH adsorption peak in stronger acids, O adsorption is indistinguishable throughout the entire testing duration in pH 2 electrolyte, likely due to a convolution of OER onset that occurs at a potential close to the adsorption potential, indicating a weakened interaction between the catalyst surface and oxygen adsorbates in pH 2. The positions of OH/O adsorption peaks also shift anodically with increasing pH after initial OER, which also suggests a less favorable surface adsorption with decreasing acidity. An inverse activity-stability relationship is also found across the tested pHs, such that electrodes in more strongly acidic environments exhibit improved OER activity but worse stability (Fig. 4c). The electrodes quickly experience performance degradation (as determined by overpotential to reach 10 mA/cm²_{geo}) after 2 h in pH 0 compared to a slower degradation process that occurs after 8 h in pH 2. Electrodes additionally display an anodic peak shift of OH/O adsorption of ~ 0.06 V and ~ 0.05 V in pH 0 and 2, respectively, over the course of total testing time compared to pristine samples (Table S3). This is followed by a phase of further degradation, when there is a sharp decrease in adsorption peak intensity such that peak locations are nonquantifiable after 4 h CA and 12 h CA in pH 0 and 2, respectively (Fig. S7). We attributed the loss of intensity and anodic shift of the adsorption peaks after extensive OER to the formation of inactive material phase with increased heterogeneity of available surface sites that makes it difficult to efficiently bind oxygenates.

To further understand how oxygenate adsorption is affected by the reaction- and environment-induced surface reconstruction, we monitor Ir dissolution for each of these electrodes after initial OER, activation, and degradation processes. Ir dissolution from the electrodes ranges from 0.5 % to 16.1 % of the total Ir loading (Fig. S8d). After initial OER, the highest Ir dissolution rate occurs in pH 0; as expected based on the reduced voltage onset of O adsorption on the catalyst surface.[15] During activation (up to 0.25 h, 2 h, and 4 h in pH 0, 1, and 2, respectively), we found Ir dissolution increases monotonically with cumulative charge passed in each electrolyte. As these electrodes generally experience higher rates of Ir dissolution during the activation period, the catalyst surface is restructuring and exposing more accessible sites to bind with oxygenates, which improves OER during this phase. After the activation period, Ir dissolution slows and stabilizes in all tested pHs. Specifically, in pH 0, the catalyst experiences a period of relative Ir stability where only an additional 0.2 % of initial Ir loading is dissolved over the next two hours. Ir leaches at a steady rate ~ 1 % per hour in pH 1 while maintaining close to 2 % for the remainder of the 12 h stability test in pH 2. Considering the anodically shifted and depressed

adsorption peaks during degradation as discussed in previous section, the more stable but less active catalyst phases formed in all pHs are correlated with unfavorable adsorbate binding. Furthermore, the electrode tested in pH 2 electrolyte doesn't exhibit significant changes in Ir dissolution over the course of testing, compared to electrodes tested in pH 0 and 1, reflecting a distinct stability regime; this is in agreement with the Pourbaix diagram of Ca_2IrO_4 (Fig. S9) which indicates that the catalyst material has a lower decomposition energy in the least acidic environment under the same operating potential.

Computational studies on IrO_2 have shown that pH influences dissolution rate and has a crucial impact on OER activity. [37,38] For Ca_2IrO_4 , we found no direct correlation between the number of Ir atoms left on the surface, surface adsorption features, and the number of reaction turnovers across electrolytes. For example, approximately the same number of Ir atoms dissolve after 0.25 h in pH 1 and 4 h in pH 2, however, neither the adsorption potential nor the intensity of OH/O adsorption matches at these corresponding conditions. Moreover, the surface formed in weaker acid supports \sim 7x increase in OER charges passed. Similarly, even though the same amount of OER charge has been passed for further degraded samples in pH 1 and 2, the sample operated in pH 0 environment lost \sim 6.5x more Ir via dissolution. Together, these results indicate that long-term operation creates a roughened and compositionally Ir-rich surface oxide phase with different reactivity and stability that influence oxygenate adsorption.

As we further consider the relationship between oxygenate adsorption and the stability of reconstructed surface, we evaluate the S-number for these electrodes, which is defined as the ratio between the amount of evolved oxygen (calculated from total OER charge) and the amount of dissolved iridium (extracted from ICP-MS data).[39] The higher the Snumber, the more stable the active center of the electrocatalyst. Here we used two methods of evaluating S-numbers to compare the stability of catalyst phases that are formed at different stages of stability testing, defined as "steady state" and "transient" S-numbers (Fig. 4d).[40] The steady-state S-number is calculated by generating a linear trendline using the total OER charge passed and amount of Ir dissolved, such that it represents behavior of the system once it has reached a steady state under reaction conditions. In contrast, the "transient" S-number is calculated based on the cumulative charge and the amount of dissolved Ir at each individual time point such that it reflects dynamic behavior of the catalyst material, especially highlighting changes during early stages of stability testing. Both methods reveal a higher S-number in higher pH, suggesting a more stable active center of the catalyst in a less acidic environment. OER performance degradation in each tested pH (after 2 h in pH 0, 4 h in pH 1, 8 h in pH 2) is associated with a similar transient S number, confirming the eventual stabilization of an inactive surface that weakens oxygenate adsorption. After initial OER, pH 2 exhibits the highest S-number and the most significant shift in OH/O adsorption peaks, indicating fast material dynamics that generate the most stable surface.

3. Conclusion

In summary, we have experimentally determined the OH and O adsorption energies on Ca_2IrO_4 nanoparticles, and correlated surface adsorption energetics of oxygenates with local atomic structure and OER kinetics during long-term operation. The local structure of Ir evolves in five stages with applied potentials, 1) deprotonation of *OH shifts Ir electronic structure to a higher average valence state, 2) increasing surface *O coverage prior to OER onset strengthens Ir-O bonding, 3) various adsorbate binding energies supported by the heterogeneous nature of Ir sites, 4) reduced site heterogeneity resulting from the activation of majority of Ir sites at high potential, 5) dynamic, reversible Ir electronic and geometric structural change with potential. The active surface that best promotes facile surface adsorbate coverage is comprised of Ir with an average valence around 4 + in stable edgesharing octahedra. After extensive OER testing, Ca_2IrO_4 experiences

severe loss of calcium and surface iridium octahedra are rearranged to a more compacted structure with a shorter average Ir-Ir bond length and increasing Ir³⁺ species. The stable but less active surface weakens the binding between catalyst and oxygenates, leading to an unfavorable formation of oxygenates that impedes OER kinetics. Comparative studies in various chemical environments show pH-dependent oxygenate adsorption that gives rise to varied OER performance. A reduced free energy barrier to oxygenate binding is correlated with improved surface reactivity and higher Ir dissolution in stronger acid. Future studies regarding the dynamic change of Ir-O structure during long-term operation requires *in situ* measurement. A deep analysis of catalyst surface structural properties with advanced electron microscopical techniques, and tools that probe both bulk and local environment will help understand complex reaction mechanisms.

Funding

This material is based upon work supported by a National Science Foundation CAREER Award (2144365-CBET).

CRediT authorship contribution statement

Ruihan Li: Writing – review & editing, Writing – original draft, Visualization, Methodology, Investigation, Formal analysis, Data curation, Conceptualization. Bingzhang Lu: Writing – review & editing, Investigation, Data curation. Jane Edgington: Writing – review & editing, Methodology, Investigation. Linsey C. Seit: Writing – review & editing, Writing – original draft, Visualization, Supervision, Resources, Project administration, Methodology, Funding acquisition, Conceptualization.

Declaration of competing interest

The authors declare that they have no known competing financial interests or personal relationships that could have appeared to influence the work reported in this paper.

Data availability

Data will be made available on request.

Acknowledgments

This work made use of the Jerome B. Cohen X-Ray Diffraction Facility supported by the MRSEC program of the National Science Foundation (DMR-2308691) at the Materials Research Center of Northwestern University and the Soft and Hybrid Nanotechnology This work made use of the EPIC and Keck-II facilities of Northwestern University's NUANCE Center, which has received support from the SHyNE Resource (NSF ECCS-2025633), the IIN, and Northwestern's MRSEC program (NSF DMR-1720139). Experimental (SHyNE) Resource (NSF ECCS-1542205). Metal analysis was performed at the Northwestern University Quantitative Bioelement Imaging Center (QBIC) generously supported by the NIH under grant S10OD020118. The authors graciously acknowledge the assistance of Rebecca Sponenburg with metal analysis at QBIC. This research used resources of the Advanced Photon Source, a U.S. Department of Energy (DOE) Office of Science User Facility, operated for the DOE office of Science by Argonne National Laboratory under Contract No. DE-AC02-06CH11357. Hard XAS measurement was performed at the DuPont-Northwestern-Dow Collaborative Access Team (DND-CAT) located at Sector 5 of the Advanced Photon Source (APS). DND-CAT is supported by Northwestern University, The Dow Chemical Company, and DuPont de Nemours, Inc. The authors also graciously acknowledge the help of Denis Keane and Qing Ma for their assistance with XAS experimentation at the 5-BM-D Advanced Photon Source.

Appendix A. Supplementary material

Supplementary data to this article can be found online at https://doi. org/10.1016/j.jcat.2024.115387.

REFERENCES

- [1] S. Shiva Kumar, V. Himabindu, Hydrogen production by PEM water electrolysis A review, Mater. Sci. Energy Technol. 2 (3) (2019) 442–454.
- [2] S. Wang, A. Lu, C.J. Zhong, Hydrogen production from water electrolysis: role of catalysts, Nano Converg. 8 (1) (2021) 4.
- [3] Sabatier, P., La catalyse en chimie organique. 2. ed., rev. et augm. ed.; Librairie polytechnique: Paris et Liege, 1920.
- [4] J. Rossmeisl, Z.W. Qu, H. Zhu, G.J. Kroes, J.K. Norskov, Electrolysis of water on oxide surfaces, J. Electroanal. Chem. 607 (1–2) (2007) 83–89.
- [5] I.C. Man, H.Y. Su, F. Calle-Vallejo, H.A. Hansen, J.I. Martinez, N.G. Inoglu, J. Kitchin, T.F. Jaramillo, J.K. Norskov, J. Rossmeisl, Universality in oxygen evolution electrocatalysis on oxide surfaces, ChemCatChem 3 (7) (2011) 1159–1165.
- [6] L.C. Seitz, C.F. Dickens, K. Nishio, Y. Hikita, J. Montoya, A. Doyle, C. Kirk, A. Vojvodic, H.Y. Hwang, J.K. Norskov, T.F. Jaramillo, A highly active and stable IrOx/SrIrO3 catalyst for the oxygen evolution reaction, Science 353 (6303) (2016) 1011–1014.
- [7] A.L. Strickler, D. Higgins, T.F. Jaramillo, Crystalline strontium iridate particle catalysts for enhanced oxygen evolution in acid, ACS Appl. Energy Mater. 2 (8) (2019) 5490–5498.
- [8] C.W. Song, J. Lim, H.B. Bae, S.-Y. Chung, Discovery of crystal structure–stability correlation in iridates for oxygen evolution electrocatalysis in acid, Energ. Environ. Sci. 13 (11) (2020) 4178–4188.
- [9] R. Zhang, N. Dubouis, M. Ben Osman, W. Yin, M.T. Sougrati, D.A.D. Corte, D. Giaume, A. Grimaud, A dissolution/precipitation equilibrium on the surface of iridium-based perovskites controls their activity as oxygen evolution reaction catalysts in acidic media, Angew. Chem. Int. Ed. Engl. 58 (14) (2019) 4571–4575.
- [10] J. Edgington, N. Schweitzer, S. Alayoglu, L.C. Seitz, Constant change: Exploring dynamic oxygen evolution reaction catalysis and material transformations in strontium zinc iridate perovskite in acid, J. Am. Chem. Soc. 143 (26) (2021) 9961–9971.
- [11] N. Li, L. Cai, G. Gao, Y. Lin, C. Wang, H. Liu, Y. Liu, H. Duan, Q. Ji, W. Hu, H. Tan, Z. Qi, L.W. Wang, W. Yan, Operando direct observation of stable water-oxidation intermediates on Ca(2–x)IrO(4) nanocrystals for efficient acidic oxygen evolution, Nano Lett. 22 (17) (2022) 6988–6996.
- [12] Z. Ma, Y. Zhang, S. Liu, W. Xu, L. Wu, Y.-C. Hsieh, P. Liu, Y. Zhu, K. Sasaki, J. N. Renner, K.E. Ayers, R.R. Adzic, J.X. Wang, Reaction mechanism for oxygen evolution on RuO2, IrO2, and RuO2@IrO2 core-shell nanocatalysts, J. Electroanal. Chem. 819 (2018) 296–305.
- [13] R.H. Zhang, P.E. Pearce, V. Pimenta, J. Cabana, H.F. Li, D.A. Dalla Corte, A. M. Abakumov, G. Rousse, D. Giaume, M. Deschamps, A. Grimaud, First example of protonation of Ruddlesden-Popper Sr2IrO4: A route to enhanced water oxidation catalysts, Chem. Mater. 32 (8) (2020) 3499–3509.
- [14] D.-Y. Kuo, J.K. Kawasaki, J.N. Nelson, J. Kloppenburg, G. Hautier, K.M. Shen, D. G. Schlom, J. Suntivich, Influence of surface adsorption on the oxygen evolution reaction on IrO2(110), J. Am. Chem. Soc. 139 (9) (2017) 3473–3479.
- [15] A.S. Raman, A. Vojvodic, Providing atomistic insights into the dissolution of rutile oxides in electrocatalytic water splitting, J. Phys. Chem. C 126 (2) (2022) 922–932.
- [16] P.E. Pearce, C.Z. Yang, A. Iadecola, J. Rodriguez-Carvajal, G. Rousse, R. Dedryvere, A.M. Abakumov, D. Giaume, M. Deschamps, J.M. Tarascon, A. Grimaud, Revealing the reactivity of the iridium trioxide intermediate for the oxygen evolution reaction in acidic media, Chem. Mater. 31 (15) (2019) 5845–5855.
- [17] N. Li, L. Cai, G.P. Gao, Y.Y. Liu, C. Wang, Z.Y. Liu, Q.Q. Ji, H.L. Duan, L.W. Wang, W.S. Yan, Origin of surface amorphization and catalytic stability of Ca2-xIrO4 nanocrystals for acidic oxygen evolution: Critical roles of acid anions, Acs Catal. 12 (21) (2022) 13475–13481.
- [18] Y.B. Chen, H.Y. Li, J.X. Wang, Y.H. Du, S.B. Xi, Y.M. Sun, M. Sherburne, J.W. Ager, A.C. Fisher, Z.C.J. Xu, Exceptionally active iridium evolved from a pseudo-cubic perovskite for oxygen evolution in acid, Nat. Commun. 10 (2019) 572.
- [19] R. Li, J. Edgington, L. Seitz, Degradation mechanism of calcium iridium oxide for oxygen evolution reaction in acid, Energy Fuel 37 (17) (2023) 13554–13561.
- [20] R.F. Sarkozy, C.W. Moeller, B.L. Chamberland, Characterization of calcium iridium oxides, J. Solid State Chem. 9 (3) (1974) 242–246.
- [21] D.Y. Kuo, H. Paik, J. Kloppenburg, B. Faeth, K.M. Shen, D.G. Schlom, G. Hautier, J. Suntivich, Measurements of oxygen electroadsorption energies and oxygen evolution reaction on RuO2(110): A discussion of the sabatier principle and its role in electrocatalysis, J. Am. Chem. Soc. 140 (50) (2018) 17597–17605.
- [22] Hummer, A. A.; Rompel, A., Chapter Eight X-Ray Absorption Spectroscopy: A Tool to Investigate the Local Structure of Metal-Based Anticancer Compounds In Vivo. In Advances in Protein Chemistry and Structural Biology, Christov, C. Z., Ed. Academic Press: 2013; Vol. 93, pp 257-305.
- [23] Z. Pavlovic, C. Rajan, Q. Gao, M. van Gastel, R. Schlogl, Probing the structure of a water-oxidizing anodic iridium oxide catalyst using raman spectroscopy, Acs Catal. 6 (12) (2016) 8098–8105.
- [24] C.W. Song, H. Suh, J. Bak, H.B. Bae, S.-Y. Chung, Dissolution-induced surface roughening and oxygen evolution electrocatalysis of alkaline-earth iridates in acid, Chem 5 (12) (2019) 3243–3259.

- [25] A. Grimaud, A. Demortière, M. Saubanère, W. Dachraoui, M. Duchamp, M.-L. Doublet, J.-M. Tarascon, Activation of surface oxygen sites on an iridium-based model catalyst for the oxygen evolution reaction, Nat. Energy 2 (1) (2016) 16189.
- [26] C. Wei, S. Sun, D. Mandler, X. Wang, S.Z. Qiao, Z.J. Xu, Approaches for measuring the surface areas of metal oxide electrocatalysts for determining their intrinsic electrocatalytic activity, Chem. Soc. Rev. 48 (9) (2019) 2518–2534.
- [27] J. Edgington, A. Deberghes, L.C. Seitz, Glassy carbon substrate oxidation effects on electrode stability for oxygen evolution reaction catalysis stability benchmarking, Acs Appl. Energy Mater. 5 (10) (2022) 12206–12218.
- [28] W. Sun, Y. Song, X.Q. Gong, L.M. Cao, J. Yang, Hollandite structure Kx approximate to 025IrO2 catalyst with highly efficient oxygen evolution reaction, Acs Appl. Mater. Inter. 8 (1) (2016) 820–826.
- [29] J.A. Arminio-Ravelo, A.W. Jensen, K.D. Jensen, J. Quinson, M. Escudero-Escribano, Electrolyte effects on the electrocatalytic performance of iridium-based nanoparticles for oxygen evolution in rotating disc electrodes, ChemPhysChem 20 (22) (2019) 2956–2963.
- [30] B. Huang, R.R. Rao, S. You, K. Hpone Myint, Y. Song, Y. Wang, W. Ding, L. Giordano, Y. Zhang, T. Wang, S. Muy, Y. Katayama, J.C. Grossman, A.P. Willard, K. Xu, Y. Jiang, Y. Shao-Horn, Cation- and pH-dependent hydrogen evolution and oxidation reaction kinetics, JACS Au 1 (10) (2021) 1674–1687.
- [31] J. Resasco, L.D. Chen, E. Clark, C. Tsai, C. Hahn, T.F. Jaramillo, K. Chan, A.T. Bell, Promoter effects of alkali metal cations on the electrochemical reduction of carbon dioxide, J. Am. Chem. Soc. 139 (32) (2017) 11277–11287.
- [32] N. Govindarajan, A.N. Xu, K. Chan, How pH affects electrochemical processes Three mechanisms underlie the impact of pH on the activity of electrochemical reactions, Science 375 (6579) (2022) 379–380.
- [33] X.Y. Liu, P. Schlexer, J.P. Xiao, Y.F. Ji, L. Wang, R.B. Sandberg, M. Tang, K. S. Brown, H.J. Peng, S. Ringe, C. Hahn, T.F. Jaramillo, J.K. Norskov, K.R. Chan, pH

- effects on the electrochemical reduction of CO(2) towards C-2 products on stepped copper, Nat. Commun. 10 (2019) 32.
- [34] B.B. Blizanac, C.A. Lucas, M.E. Gallagher, M. Arenz, P.N. Ross, N.M. Markovic, Anion adsorption, CO oxidation, and oxygen reduction reaction on a Au(100) surface: The pH effect, J. Phys. Chem. B 108 (2) (2004) 625–634.
- [35] M.E.G. Lyons, R.L. Doyle, M.P. Brandon, Redox switching and oxygen evolution at oxidized metal and metal oxide electrodes: iron in base, PCCP 13 (48) (2011) 21530–21551.
- [36] L. Giordano, B.H. Han, M. Risch, W.T. Hong, R.R. Rao, K.A. Stoerzinger, Y. Shao-Horn, pH dependence of OER activity of oxides: Current and future perspectives, Catal. Today 262 (2016) 2–10.
- [37] A. Zagalskaya, V. Alexandrov, Role of defects in the interplay between adsorbate evolving and lattice oxygen mechanisms of the oxygen evolution reaction in RuO2 and IrO2, ACS Catal. 10 (6) (2020) 3650–3657.
- [38] S. Cherevko, S. Geiger, O. Kasian, N. Kulyk, J.-P. Grote, A. Savan, B.R. Shrestha, S. Merzlikin, B. Breitbach, A. Ludwig, K.J.J. Mayrhofer, Oxygen and hydrogen evolution reactions on Ru, RuO2, Ir, and IrO2 thin film electrodes in acidic and alkaline electrolytes: A comparative study on activity and stability, Catal. Today 262 (2016) 170–180.
- [39] S. Geiger, O. Kasian, M. Ledendecker, E. Pizzutilo, A.M. Mingers, W.T. Fu, O. Diaz-Morales, Z. Li, T. Oellers, L. Fruchter, A. Ludwig, K.J.J. Mayrhofer, M.T.M. Koper, S. Cherevko, The stability number as a metric for electrocatalyst stability benchmarking, Nat. Catal. 1 (7) (2018) 508–515.
- [40] J. Edgington, L.C. Seitz, Advancing the rigor and reproducibility of electrocatalyst stability benchmarking and intrinsic material degradation analysis for water oxidation, ACS Catal. (2023) 3379–3394.